Journal of Electronic Imaging

JElectronicImaging.org

Nonscanning three-dimensional differential holographic fluorescence microscopy

David C. Clark
Myung K. Kim

SPIE. IS&T imaging.org

Nonscanning three-dimensional differential holographic fluorescence microscopy

David C. Clark* **and Myung K. Kim**
University of South Florida, Department of Physics, 4202 East Fowler Avenue, Tampa, Florida 33620, United States

Abstract. We present a technique of three-dimensional (3-D) differential imaging by the way of incoherent digital holography. We demonstrate that the method is suitable for fluorescence microscopy without the need for unfavorable scanning. We acquire the complex optical field of an incoherent volumetric scene at various times and calculate a complex difference hologram representing only the information, which has changed throughout the volumetric space during the time intervals in-between. We first demonstrate the advanced capability of self-interference incoherent digital holography combined with difference holography to track 3-D changes in a broadband, unfiltered, sunlit scene containing macroscopic continuous objects. This case is particularly remarkable due to the exceptionally short temporal coherence length and excessive build-up of noninterfering source points. We then demonstrate the ease of adaptation to the versatile, functional imaging of fluorescence microscopy. *© 2015 SPIE and IS&T* [DOI: 10.1117/1.JEI.24.4.043014]

Keywords: self-interference incoherent digital holography; differential imaging; fluorescence microscopy; incoherent holography; three-dimensional tracking.

Paper 15350P received May 5, 2015; accepted for publication Jul. 21, 2015; published online Aug. 13, 2015.

1 Introduction

Fluorescence microscopy is an indispensable imaging tool in modern biomedical research. Without the use of scanning techniques such as confocal scanning microscopy, only two-dimensional (2-D) images are captured. Confocal scanning methods have excellent depth resolution properties; however, they suffer several disadvantages, including cumbersome mechanical scanning hardware, the need to capture many separate optical sections to build up a three-dimensional (3-D) image, and increased photobleaching (and phototoxicity for biological specimens) from the necessary repeated exposure.[1,2] In contrast, a single complex hologram, recorded using a simple motionless optical system, contains sufficient information to recreate the 3-D optical field emanating from the scene, including both amplitude and phase.[3]

The 3-D recording is made possible by the interference of the object's optical field and a reference optical field, and therefore, requires coherence between the two. In Gabor's original conception, the reference is realized from a part of the illumination undisturbed by the object.[4] The invention of the laser made it possible to explicitly provide a coherent reference field.[5] Because fluorescence imaging is inherently incoherent, holography has been largely precluded from fluorescence until recent advancements.

The introduction of Fresnel incoherent correlation holography (FINCH) has fully demonstrated the ability to generate holographic images of incoherent object fields, including 3-D fluorescence microscopy.[6,7] In this technique, two copies of the object wave are superposed with different phase factors imposed by a spatial light modulator (SLM), so that every point source on the object produces the Fresnel zone interference pattern.[8] We have since developed a technique conceptually similar to FINCH called self-interference incoherent digital holography (SIDH), in which the SLM is replaced by a modified Michelson interferometer with a differential phase curvature applied by its two mirrors.[9] For continuous objects or scenes, the spatial incoherence of the object points leads to rapid build-up of an incoherent background, which is removed by standard phase-shifting digital holography.[10] The resultant hologram can then be numerically propagated to any distance to reconstruct the desired optical field.

We introduce here the process of differential self-interference incoherent digital holography (diff-SIDH). While differential holography has been an important tool in coherent holography,[11,12] it is now, for the first time, possible in incoherent holography. We demonstrate the highly effective capabilities of diff-SIDH and ease of adaptation to fluorescence microscopy. We first fully demonstrate the process on scenery of unfiltered broadband natural sunlit objects. We then demonstrate the easy adaptation to commercial grade microscopy equipment, successfully converting a professional 2-D imaging instrument into a powerful 3-D imaging and tracking tool, followed by a complete demonstration of its capabilities in fluorescence microscopy.

2 Self-Interference Incoherent Digital Holography

A basic SIDH apparatus is represented in Fig. 1. It consists of input optics and a modular SIDH configuration [a relay lens, the interferometer, and the charge-coupled detector (CCD) array]. The input optics produces an intermediate image as the input for the SIDH module. The relay lens is selected and positioned to create an appropriate final image space relative to the CCD plane (focal planes of interest should not fall directly on the recording plane for proper self-interference). The interferometer consists of a beam-splitting cube and two mirrors of different curvatures. One of these

*Address all correspondence to: David C. Clark, E-mail: dcclark@mail.usf.edu

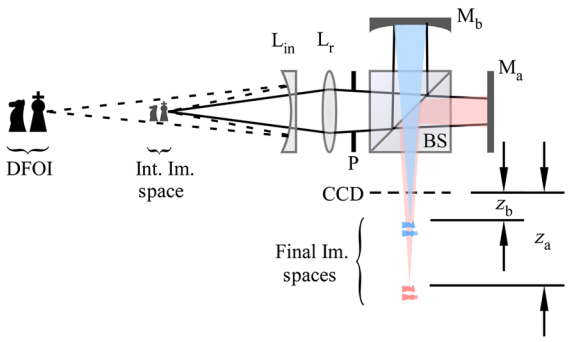

Fig. 1 Experimental diagram for self-interference incoherent digital holography (SIDH). An input lens, L_{in}, projects objects in the depth field of interest, DFOI, into the intermediate image space as input to the SIDH module. The SIDH module consists of a relay lens, L_r, an iris, P, a beam splitter, BS, a piezomounted mirror, M_a, a stationary mirror, M_b, and a CCD camera.

mirrors is mounted on a piezoactuator, which is driven by a 5-V ramp signal for full 2π phase shifting. The CCD array that is used to capture all holograms presented in this manuscript is an 800×600 pixel, 14-bit monochrome camera.

To ensure interference, the distances of the two mirrors are matched to within a margin based on the temporal coherence of the desired light source.[13] The degree of this adjustment is visibly verified by imaging a single incoherent, out-of-focus, LED source for best fringe contrast. Then several exposures of an incoherent illuminated scene are captured while the phase-shifting piezomounted mirror travels through at least one full 2π phase excursion. The complex hologram is calculated from these N intensity profiles, I_n, by

$$H = \frac{1}{N}\sum_{n=0}^{N-1} I_n e^{i2\pi\frac{n}{N}}. \tag{1}$$

It is this zero-plane (CCD plane) complex hologram, now devoid of DC and virtual twin images, that is used for further processing, such as diff-SIDH or propagation to reconstruction planes. A minimum of $N = 3$ is required to eliminate the unwanted terms; however, we chose $N = 20$ for all broadband and $N = 5$ for all fluorescent holographic experiments presented here to ensure uniform removal of the DC signal and smooth random noise effects between experiments. This resulting hologram, representing a complex optical field, is numerically propagated, as per diffraction theory,[3] by desired distances, z_h, described by

$$z_h = -\frac{z_a z_b}{z_a - z_b}, \tag{2}$$

where $z_{a,b}$ are the axial positions of the final focal planes of a desired object plane through the two paths of the interferometer and are measured relative to the CCD plane. For a well-defined optical system, these values are easily translated numerically between the object space and final holographic image space using a thin-lens approximated geometry, as well as compensation for an image shift due to the 25.4 mm BK-7 beam cube. Figure 2 shows an example of a broadband sunlit holographic scene successfully recorded by our SIDH camera using lensing and numerical aperture (NA) such that the planes of interest are visibly distinguishable. Because the coherence length is inversely proportional

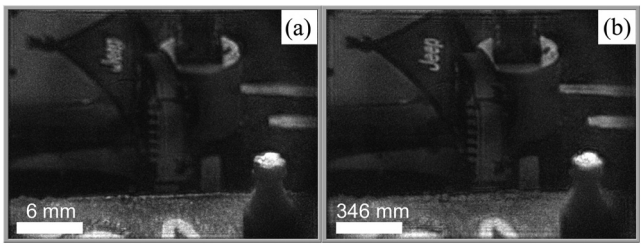

Fig. 2 A natural sunlight holographic image of an 8-mm tall rook in a window sill 60-cm away and a vehicle (Jeep) in an outside lower-level parking lot about 35 m away. The hologram is first propagated to the rook's focus plane (a), then to the Jeep's focus plane (b). Note that the scale bar has been updated to match the focus plane of interest in each case.

to bandwidth, this presents a notable challenge, which is overcome by our SIDH process. It is also worth noting here, for this obvious example, that the lateral scale of each plane of interest in a hologram changes, as will be described in Sec. 3.2.

3 Broadband Differential Incoherent Holography

3.1 *Overview of Methods and Results*

The process of diff-SIDH is applied here to the case of chess pieces on a chess board illuminated by sunlight through an office window. Referring to Fig. 1, the components of this optical system consist of $L_{in} = -75$ mm, $L_r = 50$ mm, a flat piezomounted mirror, M_a, and a 600-mm focal length curved mirror, M_b. This experiment is summarized in Fig. 3. The knight is moved from its initial position, as shown in Figs. 3(a)–3(c), to a final position shown in Figs. 3(d)–3(f). Figures 3(b) and 3(c) show the initial hologram reconstructed at the back knight and central king positions, respectively, whereas Figs. 3(e) and 3(f) show the reconstructions of the final hologram at the central king and front knight positions, respectively. A difference hologram is calculated from the unpropagated initial and final complex holograms [Figs. 3(a) and 3(d), respectively]:

$$\Delta H = H_i - H_f. \tag{3}$$

The difference hologram for this experiment is shown in Fig. 4 and contains the 3-D optical field information of the knight in both the initial and final positions, while the unchanged information, including the stationary king, are absent. In Figs. 4(a) and 4(b), this difference hologram is propagated to the same back and front knight positions used for Figs. 3(b) and 3(f), respectively, demonstrating that this information has been preserved. It can also be noted that information on the chess board, both overlap and specular reflection from the knight, is also preserved in a difference hologram, since this represents changed information as well.

3.2 *Detailed Analysis and Discussion*

From the single complex operation in Eq. (3), the overall volumetric change of source points making up the scene is computed and movement of the object points in the scene is determined in three dimensions. For any point, or group of points such as an object, a 3-D displacement vector can be calculated describing the movement between the time

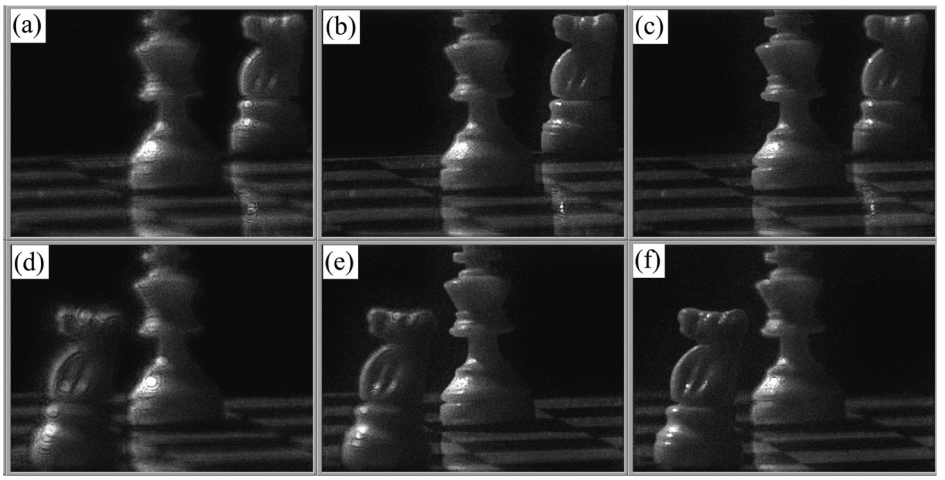

Fig. 3 Sunlit initial and final complex holograms for diff-SIDH. Chess pieces, knight and king, were arranged as shown in the initial hologram, (a–c). The knight was then moved to a new position and a final hologram was recorded, (d–f). (a), (b), and (c) are the same initial hologram at the zero-plane (unpropagated), the knight plane, and the king plane, respectively. (d), (e), and (f) are the final hologram at the zero-plane, the king plane, and the new knight plane, respectively.

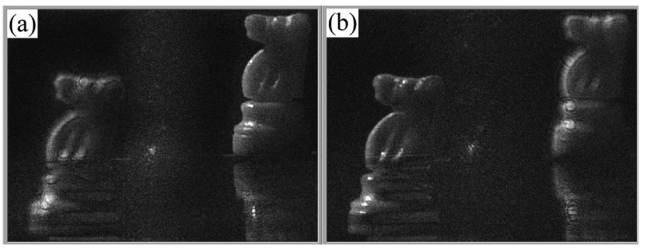

Fig. 4 Differential hologram containing the 3-D information of the changes only. (a) Numerically propagated to the initial knight plane and (b) to the final knight plane.

of the initial and final holograms. In the present case, if we select the eye of the knight as an easy point of reference, a 3-D displacement vector can be calculated showing the projected path between the two positions. Using the plane parallel to the CCD plane that contains the initial eye as our initial reference and setting the origin on the optical axis, i.e., at the center of our two-dimensional field of view (FOV), position vectors can be constructed from the difference hologram for the initial and final eye positions by

$$\mathbf{v}_n = \left[\frac{px_n}{X}x_n, \frac{py_n}{Y}y_n, z_n\right], \tag{4}$$

where px and py are the lateral pixel position coordinates, X and Y are the lateral FOV's in pixels, and x_n and y_n represent the object space FOV's in units of length. This object space FOV is, of course, scaled based on the depth plane of interest at z_n by the relation:

$$x_n = x_0\left(\frac{z_0 - z_n}{z_0}\right) \tag{5}$$

(and identically for y_n), where x_0 is the known object space FOV at a plane located at z_0, and z_n is measured from this z_0 plane and is translated from z_h, as described in the following paragraph. For our example, applying Eqs. (4) and (5), we have

$$\begin{aligned}\Delta\mathbf{v} &= \mathbf{v}_2 - \mathbf{v}_1 \\ &= [-5.4, 2.5, 62]\ \text{mm} - [8.9, 7.1, 0]\ \text{mm} \\ &= [-14.3, -4.6, 62]\ \text{mm}\end{aligned} \tag{6}$$

for the knight's displacement vector in object space. While this result is reasonably well verified, by design this example lacks a well-defined optical axis relative to the scene, so we will reserve in-depth analysis for more appropriate experiments in Sec. 4. Consequently, we will use this example to introduce and describe some important concepts before moving forward.

It is important to consider the relative locations of the subjects of interest, i.e., the depth field of interest (DFOI). Since we are interested in tracking objects in a 3-D volume of space, our intermediate image space should consist of an appropriate volume of space as input for the diff-SIDH system. In the above experiment, the DFOI (spanning approximately the axial length of the chess board) is between 350 and 430 mm from the relay lens. This DFOI is translated through the input and relay optics and the interferometer to the ranges, z_a and z_b, of 25.7 to 39.8 mm and 7.62 to 17.4 mm, respectively. Thus, applying Eq. (2), we expect objects in our DFOI to come into focus within the propagation range, z_h of −10.8 to −30.8 mm. Of course, these relationships are nonlinear and a numerical simulation of our constructed system produces a translation from object space DFOI into final holographic propagation space as plotted in Fig. 5(a). Specifically, our three object positions of interest consisting of the 425-mm back knight position, the 401-mm king position, and the 363-mm forward knight position are predicted to be in focus at propagation distances: −11.7, −16.3, and −26.4 mm, respectively. These three predicted propagation planes were chosen for display in Figs. 3(b), 3(c), 3(e), and 3(f), respectively. Clearly, these are appropriate planes for the objects in question.

While the choice of lensing is quite important for defining the DFOI for a given application, it is the NA that is most directly related to the system's depth resolution. Incorporating an appropriate NA for the current demonstration

did not pose a noteworthy challenge; however, we believe that it is important to discuss the relationship to these results, at least in brief, as it is an important parameter for other applications. We are able to see, qualitatively, that our holograms can distinguish between the object planes of interest due to the degree of blur that exists in the out-of-focus planes. This blur is described by a parameter known as the circle of confusion, c, which is proportional to NA by

$$c = \frac{2\mathrm{NA}|z - z_0|f}{z}, \tag{7}$$

where f is the lens focal length, z_0 is the position of the in-focus plane, and z is the position of an out-of-focus plane. The expected blur in units of pixels versus object space for a standard (nonholographic) image of our DFOI with the king plane set to in-focus is plotted in Fig. 5(b). A qualitative comparison with Figs. 3(c) and 3(e), which are numerically propagated to this plane, shows that the relationship here is reasonable. For now, we will use this relationship to describe the general importance of such a parameter in defining depth resolution. If we consider a generic focus algorithm for digital imaging, it will be limited in some way by units of pixels such as we have used here. For the sake of our qualitative comparison, we may assign the minimum of one pixel of blur before we detect an edge to be out of focus; thus, our depth resolution would be 4.9 mm in object space for the region about the king plane. Note that because the NA varies with the object plane, the depth resolution will also change depending on the target within the hologram.

As mentioned earlier, a major challenge in applying SIDH to broadband sunlit scenery is the severely reduced temporal coherence. Careful consideration should be taken of image space NA and mirror geometry to ensure that optical path differences between self-interfering points will remain

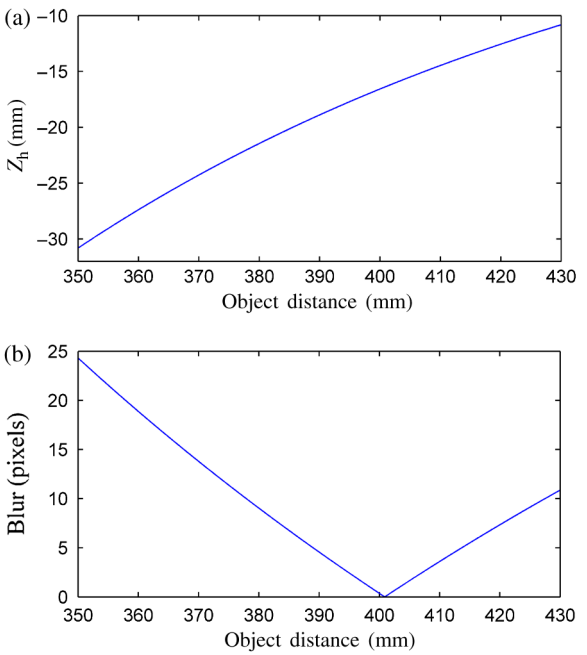

Fig. 5 Space and blur predictions. (a) Numerical simulation showing the holographic propagation distances, z_h, expected for object planes within the DFOI. (b) Expected image blur in pixels for objects in the DFOI when the king plane (401 mm away) is brought into focus.

mostly within this coherence envelope even during phase shifting. First, comparing a plane mirror and a curved mirror from a geometric standpoint, some path variation, δ, will be applied due to the curvature difference described by

$$\delta = 2f - \sqrt{4f^2 - r^2}, \tag{8}$$

where f is the focal length of the curved mirror and r is some radial distance from the vertex (assuming here that this vertex is on the optical axis and conjugate with the plane mirror of the alternate path). Clearly, from Eq. (8), this variation can be reduced by limiting the optical field diameter at the mirror plane. This is easily achieved by reducing the image space NA, such as by iris adjustment. In fact, minimizing this field diameter at the mirror plane to that necessary to fill the CCD may significantly reduce the DC build-up, as well as random nonharmonic effects,[14] putting less strain on the phase-shifting process allowing for quicker capture rates with fewer necessary exposures per hologram [N in Eq. (1)]. Alternatively, or in tandem to this option, the plane mirror can be replaced by a second curved mirror, provided differential curvature between the two is maintained. The path variation due to the mirrors then becomes the difference between the variations, $\delta_{a,b}$, for each curved mirror of focal length, $f_{a,b}$.

We would like to briefly comment on chromatic dispersion for the broadband qualitative experiments presented above. Equation (1) is valid for the period, i.e., the 2π excursion, which is dependent on a representative wavelength of the illumination. For this unfiltered case, it was reasonable to assume a representative wavelength of the resulting monochromatic complex hologram of the black and white object scene to be 550 nm for the subsequent diffraction. If a more quantitative approach is desired, a narrow band filter can be applied to minimize dispersion. In fact, tricolor filtering, in which each band is processed separately, can be performed to reconstruct full-color holograms from natural light.[15]

While some of the noted constraints have prompted a necessary compromise for the challenging broadband application presented in this section, it must be noted that other, much more significant, applications may impose no substantial compromise. Fluorescence microscopy, for example, involves narrow-band emission and often point-source-like structures, which are much less constraining on the SIDH module promoting substantially higher rates of holographic capture and greater freedom in NA.

4 Differential Holographic Fluorescence Microscopy

4.1 *Overview of Methods and Results*

In preparation for working with fluorescence microscopy materials and instruments, we fabricated a modular SIDH system which we mount directly to the camera port of standard commercial microscopes. In essence, referring to Fig. 1, the input lens, L_{in}, is replaced by the microscope as an input device to generate the intermediate image space for the SIDH module. In this way, bright-field or fluorescent microscope images are successfully recorded as complex holograms containing the 3-D volumetric information of the object space extending above and below the microscope's normal input

plane. This SIDH module has a relay lens, $L_r = 40$ mm, and mirror pair, M_a and M_b, of focal lengths 100 and 75 mm, respectively.

In this section, the module is applied to the camera port of a commercial microscope which has been set up to allow for fluorescence excitation by a 532-nm laser applied at an oblique angle to avoid direct illumination into the objective. We use 1.0-μm beads labeled with a fluorophore of 540-nm peak excitation and 560-nm peak emission and apply a 560-nm band pass filter to the imaging side. A separate translation stage is constructed for controlled 3-D translation of a coverslip containing fixed beads, while a thin bead matrix, frozen in a polyacrylamide gel, remains stationary on the microscope stage. Due to the narrow band, the number of frames used for phase shifting was reduced to 5, thus improving the holographic capture speed.

A summary of this experiment is shown in Fig. 6. Figures 6(a)–6(c) represent the initial, final, and difference holograms, respectively, all propagated to a plane located within the stationary gel matrix of beads. Notice that at this plane, that the static bead matrix, principally in-focus, is present in Figs. 6(a) and 6(b), but is absent in Fig. 6(c), while the bead groupings from the more distant translated coverslip are individually visible as out-of-focus projections in Figs. 6(a) and 6(b) and together in Fig. 6(c). The same holograms appearing in Figs. 6(a) and 6(b) are shown in Figs. 6(d) and 6(e), but are now reconstructed on the initial coverslip plane and the final translated coverslip plane, respectively. Figures 6(f) and 6(g) show the same difference hologram [Fig. 6(c)] reconstructed on the same plane as in Fig. 6(d), then on the same plane as in Fig. 6(e), respectively. Thus, the difference hologram has successfully maintained only the information on the distant fluorescent bead groupings, which were translated during the time interval.

4.2 *Detailed Analysis and Discussion*

By applying an SIDH module to a commercial microscope, we no longer have knowledge of the optical components of our entire system. While the SIDH module is known and characterized, the enclosed microscope system remains unknown. It is, therefore, not feasible to numerically simulate this system as a whole in order to translate back and forth between object space and the final holographic space for the purpose of depth analysis. Fortunately, we can derive the necessary relationship for the unknown optical system.

It is not necessary, or particularly useful, to predict an object location in reference to a part of the imaging system, such as the microscope objective or a principal plane, but only in reference to other object positions within the sample of interest. We, therefore, look only at the differentiable relationship of the object space and image space for the unknown system, the microscope. We will derive this relationship here by treating the microscope as a set of two unknown lenses; however, the important aspects of the result hold true for a system of any number of unknown elements. From geometric optics considerations, we start with the relationship between object space, z_o, and final image space, z_i, for this system:

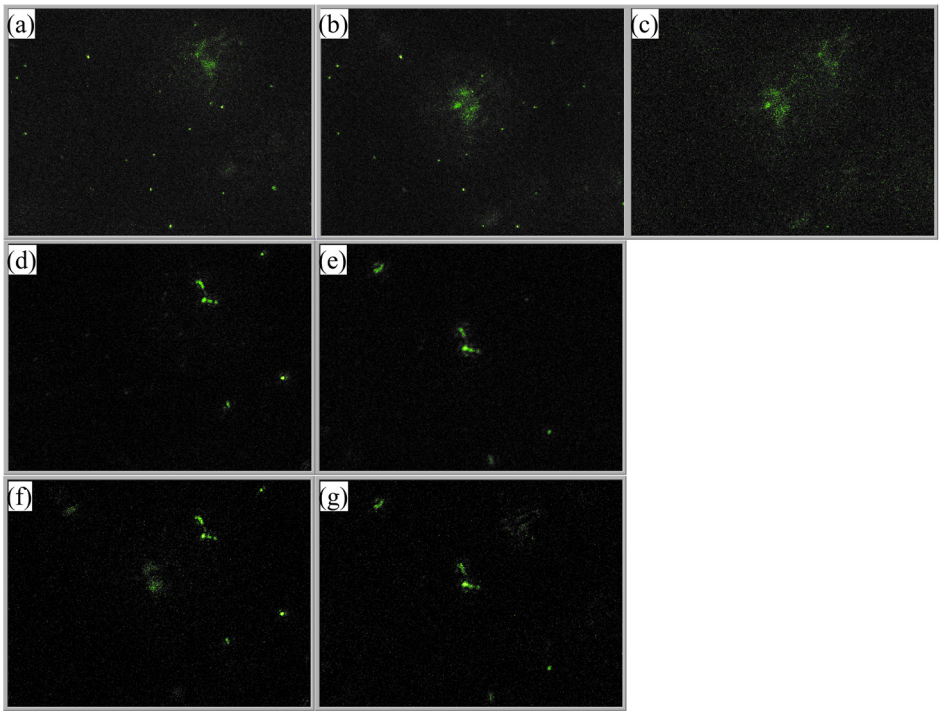

Fig. 6 Differential SIDH fluorescence microscopy with translational and stationary bead layers (pseudocolor). (a), (b), and (c) represent the initial, final, and differential holograms, respectively, all reconstructed at a plane of the stationary bead matrix. (d) and (e) are the same holograms, (a) and (b), respectively, but now reconstructed at the initial and final z-translated bead position planes, respectively. The difference hologram, (c), is likewise reconstructed to these initial and final z-translated planes (f) and (g), respectively. Note, for the difference hologram, the absence of the stationary matrix and the presence of both positions of the translated beads.

$$z_o = \frac{f_1[d - f_2 z_i/(z_i - f_2)]}{d - f_1 - f_2 z_i/(z_i - f_2)}, \tag{9}$$

where f_1 and f_2 are the lens focal lengths and d is the distance between them. Differentiating with respect to final image space, we get

$$\frac{dz_o}{dz_i} = -\frac{f_1^2 f_2^2}{[-f_1 f_2 - d f_2 + (-d + f_1 + f_2) z_i]^2}. \tag{10}$$

The inverse relationship then takes on the form:

$$\frac{\Delta z_i}{\Delta z_o} \equiv a + b z_i + c z_i^2, \tag{11}$$

where the constants a, b, and c are entirely defined by the constants of the unknown system. An iterative exercise of the chain rule applied in Eq. (10) will show that Eq. (11) holds for any number of elements that may be hidden within the unknown system. Note, also, that the unknown position of the principal planes is of no consequence to these relations. Since our SIDH module is known, a calibration experiment can be performed on the microscope to allow translation between the object and final holographic space through the shared intermediate image space, z_i, by fitting the second-order polynomial solution to the calibration data.

We perform this calibration experiment by recording holograms of a selected fluorescing bead, or group of beads, while translating in controlled steps along the z-axis. We then determine the best focus z_h value, by the method described in the following paragraph, for each controlled z_o step. The appropriate z_i is converted from each z_h and $\Delta z_i/\Delta z_o$ is calculated between each step. Figure 7 shows the resulting prediction curve compared to the input calibration data.

To test the success of this prediction curve, we perform a multistep controlled diff-SIDH experiment. A new fluorescent bead of interest is positioned toward the left of the FOV at some starting position relatively close to the microscope objective and translated in steps of $\Delta x = 20\ \mu$m (toward the right) and $\Delta z = -12.7\ \mu$m (away from the objective) while a hologram is recorded at each step. Then a series of differential operations are performed as described by Eq. (3), where the resulting ΔH of each step becomes H_i for the next step. This produces a single difference hologram containing all of the recorded positions of the reference bead [Figs. 8(a) and 8(b)]. A horizontal selection line passing through each position of the bead is used for a numerical depth scan to determine the appropriate z_h value for each position [Fig. 8(c)]. In order to select the best representative values, a Gaussian model is fit to each position, as shown in Fig. 9. The result of this peak selection (the Gaussian parameter describing the mean) is then plotted on the prediction curve in Fig. 10. Now, selecting the best representative lateral position values similarly [Figs. 9(c) and 9(d)], the results are tabulated for all six positions of this bead in Table 1.

We should note here, as mentioned in Sec. 3.2, the precision with which we determine the lateral and axial values varies with the axial plane of interest. This is easily recognized, particularly for the axial component, by the difference in Gaussian distributions in Fig. 9 for the six bead positions. We can relate these distributions, statistically, to the level of confidence with which we report the peak values. For example, by the central limit theorem, we know that the standard deviation in the mean is related to that of the whole distribution by:[16]

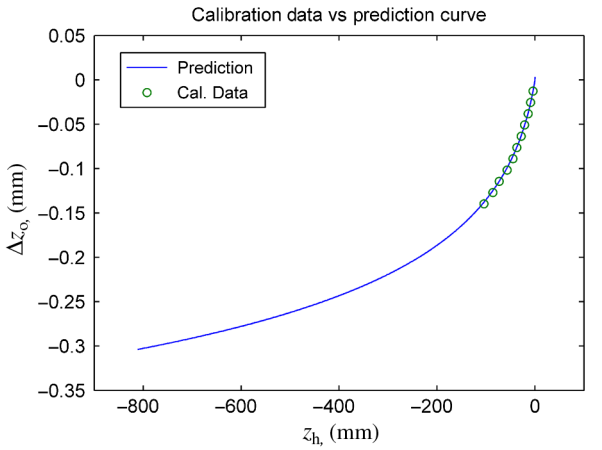

Fig. 7 Calibration versus prediction. The collected calibration data are used to produce the extended prediction curve relating holographic propagation to axial object space position through an unknown optical system.

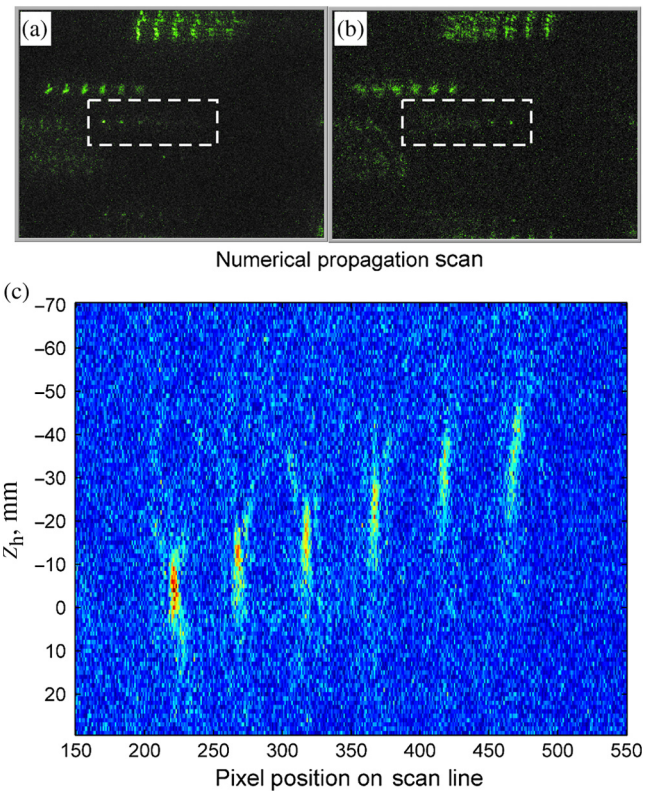

Fig. 8 Multistep diff-SIDH fluorescence microscopy (pseudocolor). An iterative series of differential operations for an x- and z-translated fluorescent bead of interest (indicated by dashed box) results in the difference hologram, (a) and (b), containing all six positions. (a) and (b) represent reconstruction at the first and last of the six bead positions, respectively. (c) A numerical propagation scan of the hologram through z_h showing the reconstruction of a selection line passing through all bead positions.

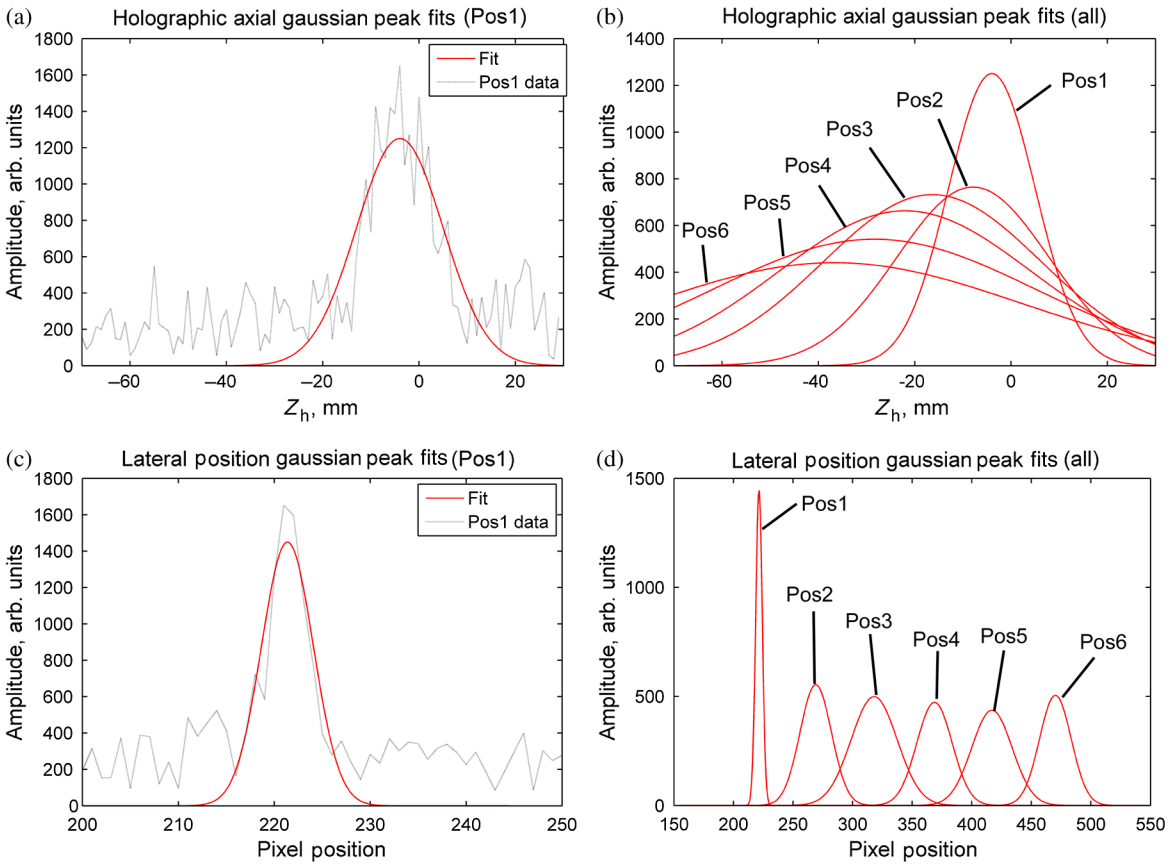

Fig. 9 Gaussian fit peak selection. (a) An example plot showing the comparison of the holographic propagation, z_h, scan data for bead position 1 with its Gaussian fit. (b) Results of Gaussian fits for all six z_h bead positions. (c) The lateral pixel position data for position 1 with its Gaussian fit. (d) Results of Gaussian fits for all six lateral bead positions.

$$\sigma_m = \frac{\sigma}{\sqrt{n}}, \tag{12}$$

where σ is the standard deviation determined from the Gaussian fit and n is the number of samples used to produce the fit. From this relation, we see that as σ increases for more distant planes, it may be necessary to improve sampling resolution, and thus increase n to help compensation.

Table 1 Multistep differential self-interference incoherent digital holography fluorescent bead positions.

Experimental $[x, z]$ shift (μm)	Lateral pixel position	Lateral object shift (μm)[a]	z_h value (mm)	Axial object shift (μm)[b]
[0, 0]	221.4	0	−4.0	0
[20, −12.7]	269.0	19.3	−7.9	−10.3
[40, −25.4]	318.0	39.2	−16.3	−28.6
[60, −38.1]	368.7	59.8	−22.0	−39.1
[80, −50.8]	417.0	79.5	−28.4	−50.3
[100, −63.5]	470.2	101.2	−36.7	−62.3

[a]Determined from Eqs. (4)–(6) and relative to initial position.
[b]Determined from z_h value on prediction curve.

Remember that the depth scan sampling resolution is selected in postprocessing of the already recorded hologram and is completely numerical, thus it does not affect or constrain the optical system whatsoever.

Finally, returning to our layered fluorescence diff-SIDH experiment from Sec. 4.1 (Fig. 6), we determine a meaningful displacement vector of the translated group of beads.

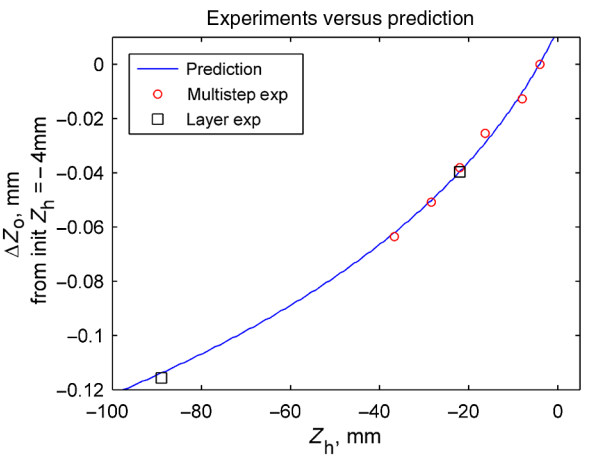

Fig. 10 Experiments versus prediction. Data from both the layered (Fig. 6) and multistep (Fig. 8) fluorescence diff-SIDH experiments are plotted with the prediction curve (Fig. 7) for comparison. The experimental points consist of the intended z-translation in object space and the Gaussian fit peak determined best focus value for z_h.

First, selecting a bead of reference in the translated bead group, then applying the numerical propagation scan, axial, and lateral Gaussian peak fitting, and finally Eqs. (4)–(6), we get the displacement vector, $[-51.0\mathbf{x}, -51.1\mathbf{y}, -74.0\mathbf{z}]$ μm. We compare this with the intended translation of $[-50\mathbf{x}, -51\mathbf{y}, -76\mathbf{z}]$ μm. We plot, in Fig. 10, this experiment's fit-determined z_h values of -22 and -89 mm for the initial and final positions, respectively, and the intended object space z-translation for comparison with the prediction curve and find acceptable agreement.

5 Discussion and Conclusion

We have demonstrated that our SIDH process can bridge the gap between 3-D holographic imaging and existing incoherent imaging technologies spanning telescopy, photography, and microscopy from broadband sunlight to functional fluorescence. Our SIDH method has the advantages of speed, simplicity, and reduced risk of photodamaging effects over scanning technologies and because an interferometer is used in place of an SLM, SIDH is much more cost effective to implement than the competing FINCH technology. By combining SIDH with differential holography, we have demonstrated the ability of a single complex operation to efficiently and effectively catalog 3-D changes in a crowded volumetric scene. Additionally, by briefly demonstrating the use of numerical peak-finding methods for 3-D point location, we suggest that the entire process is suitable for automation for applications of machine vision as well.

Our near future aim is to record 3-D fluorescence profiles and track florescent tags in living organisms without the use of phototoxic raster scanning. Even without a change in position, our method may also be sensitive to fluorescence intensity changes due to ligand binding and molecular conformation changes, which has been of interest.[17,18] Additionally, we aim to improve the measurement precision of the biological cell traction force previously measured by quantitative phase imaging of surface wrinkles caused by cellular movement.[19] In this case, a fluorescent bead matrix in a deformable gel substrate will be tracked by differential fluorescence holography during cellular motion across the substrate, such that small variations of the bead positions are related to cellular traction force.

Although we have demonstrated significantly improved holographic capture rates for narrowband applications, we are currently developing a single-shot, off-axis SIDH method, which will eliminate the need for phase shifting by incorporating a slight tilt between the self-interfering copies.[20] This may be quite significant for dynamic biological applications, where temporal resolution is important as well as vastly improved frame rates for 3-D holographic video photography.

Acknowledgments

We would like to thank Dr. Byeong Cha from the Department of Molecular Pharmacology & Physiology of University of South Florida Morsani College of Medicine for his helpful input on biological and fluorescence applications.

References

1. R.-A. Lorbeer et al., "Highly efficient 3D fluorescence microscopy with a scanning laser optical tomograph," *Opt. Express* **19**, 5419–5430 (2011).
2. P. A. Santi, "Light sheet fluorescence microscopy: a review," *J. Histochem. Cytochem.* **59**, 129–138 (2011).
3. M. K. Kim, *Digital Holographic Microscopy: Principles, Techniques, and Applications*, Springer, New York (2011).
4. D. Gabor, "A new microscopic principle," *Nature* **161**(4098), 777–778 (1948).
5. E. N. Leith and J. Upatnieks, "Wavefront reconstruction with continuous-tone objects," *J. Opt. Soc. Am.* **53**, 1377–1381 (1963).
6. J. Rosen and G. Brooker, "Non-scanning motionless fluorescence three-dimensional holographic microscopy," *Nat. Photonics* **2**, 190–195 (2008).
7. J. Rosen and G. Brooker, "Fluorescence incoherent color holography," *Opt. Express* **15**, 2244–2250 (2007).
8. J. Rosen and G. Brooker, "Digital spatially incoherent Fresnel holography," *Opt. Lett.* **32**, 912–914 (2007).
9. M. K. Kim, "Incoherent digital holographic adaptive optics," *Appl. Opt.* **52**, A117–A130 (2013).
10. I. Yamaguchi and T. Zhang, "Phase-shifting digital holography," *Opt. Lett.* **22**, 1268–1270 (1997).
11. L. O. Heflinger, R. F. Wuerker, and R. E. Brooks, "Holographic interferometry," *J. Appl. Phys.* **37**, 642–649 (1966).
12. P. Naulleau et al., "Detection of moving objects embedded within scattering media by use of speckle methods," *Opt. Lett* **20**, 498–500 (1995).
13. F. Dubois et al., "Digital holographic microscopy with reduced spatial coherence for three-dimensional particle flow analysis," *Appl. Opt.* **45**, 864–871 (2006).
14. F. Le Clerc, L. Collot, and M. Gross, "Numerical heterodyne holography with two-dimensional photodetector arrays," *Opt. Lett.* **25**, 716–718 (2000).
15. M. K. Kim, "Full color natural light holographic camera," *Opt. Express* **21**, 9636–9642 (2013).
16. M. L. Boas, *Mathematical Methods in Physical Sciences*, 2nd ed., Wiley, New York (1983).
17. S. D. Jhaveri et al., "Designed signaling aptamers that transduce molecular recognition to changes in fluorescence intensity," *J. Am. Chem. Soc.* **122**, 2469–2473 (2000).
18. C. Eggeling et al., "Monitoring conformational dynamics of a single molecule by selective fluorescence spectroscopy," *Proc. Natl. Acad. Sci.* **95**, 1556–1561 (1998).
19. X. Yu et al., "Measurement of the traction force of biological cells by digital holography," *Biomed. Opt. Express* **3**, 153–159 (2012).
20. J. Hong and M. K. Kim, "Single-shot self-interference incoherent digital holography using off-axis configuration," *Opt. Lett.* **38**, 5196–5199 (2013).

David C. Clark is a research scholar at the University of South Florida. He received his PhD in applied physics at the University of South Florida in 2012. He has authored 27 journal and conference publications, several by invitation. His current research interests are applications of incoherent digital holography in microscopy, telescopy, and 3-D photographic sensing. He is a member of SPIE and OSA.

Myung K. Kim is a professor of physics at the University of South Florida. He received his PhD from the University of California, Berkeley, in 1986. His current research interests are in digital holography, microscopy, biomedical imaging, 3-D imaging, and holographic adaptive optics. Of particular interest and recent focus is holography of incoherent light and applications in 3-D fluorescence microscopy. He is a fellow of OSA and a senior member of SPIE.